Thermoelectric transport properties of ferromagnetic graphene with *CT*-invariant quantum spin Hall effect

Miaomiao Wei,[1,2] Min Zhou,[1,2] Bin Wang,[3,*] and Yanxia Xing[1,2,†]

[1]*Key Laboratory of Advanced Optoelectronic Quantum Architecture and Measurement, Ministry of Education, Beijing Institute of Technology, Beijing 100081, China*

[2]*Beijing Key Laboratory of Nanophotonics and Ultrafine Optoelectronic Systems, Beijing Institute of Technology, Beijing 100081, China*

[3]*Shenzhen Key Laboratory of Advanced Thin Films and Applications, College of Physics and Optoelectronic Engineering, Shenzhen University, Shenzhen 518060, China*

(Received 7 February 2020; revised 19 June 2020; accepted 27 July 2020; published 17 August 2020)

We investigate thermoelectric transport properties of ferromagnetic graphene with *CT*-invariant quantum spin Hall (*CT*-QSH) effect. Considering a strong magnetic field, we calculate the charge Seebeck coefficient S_c, spin Seebeck coefficient S_s, charge Nernst coefficient N_c, and spin Nernst coefficient N_s based on the nonequilibrium Green's function and Landauer-Büttiker formula. Due to the coexistence of the *CT*-QSH and quantum Hall (QH) effects in ferromagnetic graphene, thermoelectric coefficients are divided into the QSH and QH types appearing at the zeroth and nonzero Landau levels, respectively. We find both the charge thermoelectric coefficients are determined by the filling factor ν_σ. The nth peak heights of the QH-type N_c and S_c satisfy $|S_{c,n}| = N_{c,n} = \ln 2/(|n| + \frac{1}{2})$, exhibiting the half-integer QH effect. However, the mth peak height of the QSH-type N_c satisfies $N_{c,m} = \ln 2/|m|$, similar to the integer QH effect. The peak height of N_s remains $N_s = \mathrm{sgn}(s)2\ln 2$, and its sign depends on the spin of Landau level, either the QH or QSH type. In addition, the peak height of the QH-type S_s remains $2\ln 2$. In the clean system, the QSH-type S_c and S_s are zero, while the QSH-type N_c and N_s appear at the zeroth Landau levels, which is different from the zero N_c and N_s in the conventional QSH system. In the presence of disorders, the QH-type thermoelectric coefficients are more robust than the QSH. For the QH-type thermoelectric coefficients, S_c and S_s are more robust than N_c and N_s. Notably, the QSH-type S_c and S_s are no longer zero in dirty systems.

DOI: 10.1103/PhysRevB.102.075432

I. INTRODUCTION

Thermoelectric transport, originating from the balance between the electric and thermal forces acting on the charge carriers, describes the thermoelectric power induced by the temperature gradient, as manifested in the Seebeck and Nernst effects. With the combination of spin, the spin Seebeck and spin Nernst effects have attracted considerable attention, which creates an emerging research field, namely, spin caloritronics [1]. Generally, the Seebeck- and Nernst-type coefficients are measured in two- and four-terminal devices, respectively. During the past few decades, the development of low-temperature measurement technology and microfabrication technology have made it possible to precisely measure thermoelectric transport signals in various systems, such as bismuth [2], quantum dot [3,4], superconductors [5,6], carbon-based structures [7], molecular junctions [8], and so on. The spin Seebeck [9–11] and spin Nernst effects [12,13] can also be precisely measured due to the development of spin-detection techniques. Furthermore, spin thermoelectric transport is also theoretically investigated in various systems, such as ferromagnetic heterojunctions [14], quantum dot [15], two-dimensional electron gas [16], molecular junction [17,18], and antiferromagnets [19,20].

Thermoelectric coefficients are more sensitive to the details of the density of states than the conductance [21,22], which is very crucial for the design of electronic devices. Thermoelectric transport in the quantum Hall (QH) and quantum spin Hall (QSH) systems provides a way to reduce the generation of heat and improve the efficiency of thermoelectric conversion [23–25], which have attracted great theoretical [26–28] and experimental [29–31] interest. Graphene possesses a unitary band structure, and the conductivity depends linearly on the charge carriers in experiment [32]. Particularly, magnetic graphene has a considerably large figure of merit for spin thermoelectric power, making it a potential material for spin caloritronics [33]. Through injecting a spin-polarized current [34,35] or using an insulating ferromagnetic substrate [36], ferromagnetic graphene is realized. Then if a strong perpendicular magnetic field is further applied, the *CT*-QSH effect will appear [37]. Unlike the conventional QSH effect derived from the spin-orbit interaction (SOI) and protected by the time-reversal (T) invariance [38], the *CT*-QSH effect appears in the absence of SOI and is protected by the *CT* invariance, where C is the charge conjugation operation. In addition, the *CT*-QSH and QH effects coexist in ferromagnetic graphene under a strong magnetic field. It is imperative to quantitatively explore the thermoelectric transport properties in such

*binwang@szu.edu.cn
†xingyanxia@bit.edu.cn

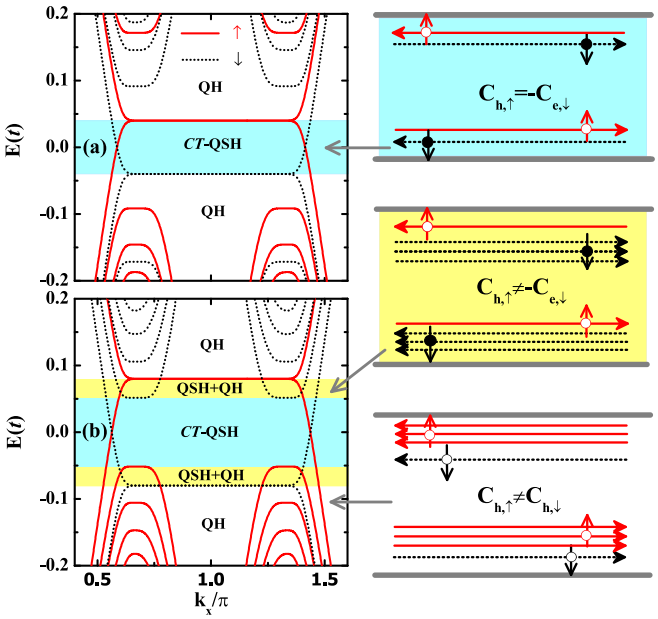

FIG. 1. Energy bands of ferromagnetic graphene nanoribbon with exchange field (a) $M = 0.04t$ and (b) $0.08t$. The other parameters are magnetic field $\phi = 0.005$, ribbon width $N = 40$. The cyan, yellow, and white denote the *CT*-QSH, QSH + QH, and QH regions, respectively. The right panels show the edge states of each region.

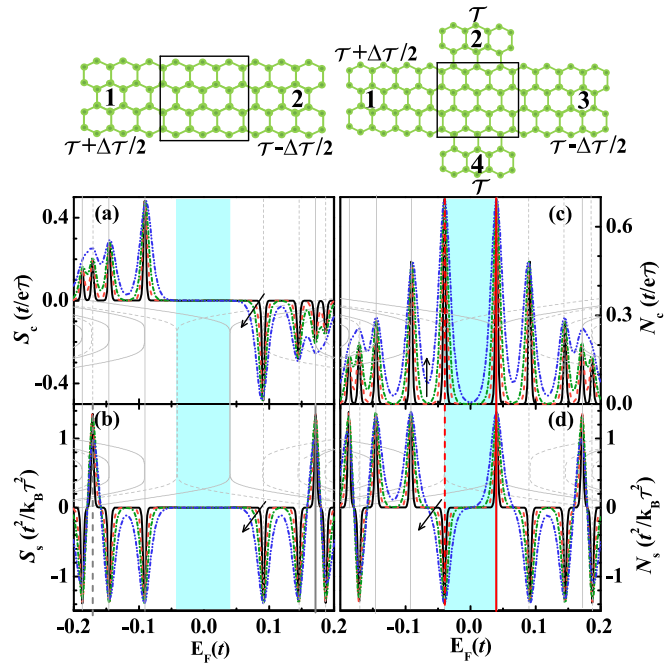

FIG. 2. The two-terminal device and the corresponding (a) S_c and (b) S_s vs Fermi energy E_F. The four-terminal device and the corresponding (c) N_c and (d) N_s vs Fermi energy E_F. The other parameters are exchange field $M = 0.04t$, magnetic field $\phi = 0.005$, scattering width $N = 40$, and length $L = 40$. Along the black arrow, each line represents a different temperature $k_B\mathcal{T} = 0.001t, 0.002t, 0.003t, 0.005t$.

a unique system, which will help to improve the conversion efficiency between the thermal and electrical energies.

In this paper we study the thermoelectric effect of ferromagnetic graphene under a strong magnetic field in which the *CT*-QSH and half-integer QH effects coexist. Here the *CT*-QSH effect is distinguished from the conventional QSH effect originated from SOI. The former corresponds to a multiband-gap structure, while the latter is the result of a nontrivial single band gap. This discrepancy in the details of band structure is reflected in the thermoelectric transport processes. Therefore we focus on the charge Seebeck coefficient S_c, spin Seebeck coefficient S_s, charge Nernst coefficient N_c, and spin Nernst coefficient N_s. Novel thermoelectric transport properties appear at Landau levels, and thermoelectric coefficients are divided into the QSH and QH types when Fermi energy crosses the zeroth and nonzero Landau levels, respectively. The QSH-type S_c and S_s are zero in the clean system because the two-terminal device cannot feel the change of chirality of the edge state. However, the QSH-type N_c and N_s appear at the zeroth Landau level, i.e., the boundary between the *CT*-QSH (QSH + QH) and QH regions in Figs. 1(a) and 1(b). This is different from the conventional QSH system, in which the information about the bulk density of states is missing in the nontrivial band gap, not only S_c and S_s, but also N_c and N_s are all zero. In return, we can use thermoelectric transport signals to distinguish the *CT*-QSH effect and half-integer QH effect. The peak height of the QSH-type N_c varies with exchange field M and satisfies $N_{c,m} = \ln 2/|m|$, with $m = 1, 2, ...$, similar to the integer QH effect. The nth peak heights of the QH-type S_c and N_c satisfy $S_{c,n} = -\mathrm{sgn}(c)\ln 2/(|n| + \frac{1}{2})$ and $N_{c,n} = \ln 2/(|n| + \frac{1}{2})$ with $n = 1, 2, ...$, corresponding to the half-integer QH effect, where $\mathrm{sgn}(c)$ represents the sign of charge. However, the peak height of the QH-type $|S_s|$ remains $2\ln 2$. Different from the peak height of N_c that depends on the filling factor ν_σ, the peak height of $|N_s|$ is always $2\ln 2$, either the QH or QSH type, and N_s and S_s can be positive or negative depending on the spin σ of filling factor ν_σ. Finally, in the presence of disorders, the helical edge states are broken. Instead of the zero values in the clean system, the QSH-type S_c and S_s begin to appear.

The rest of the paper is organized as follows. In Sec. II we introduce the effective tight-binding Hamiltonian of ferromagnetic graphene under a strong perpendicular magnetic field and the formulas for calculating the thermoelectric coefficients. In Sec. III, we present the numerical results and relevant discussions. Finally, a conclusion is given in Sec. IV.

II. HAMILTONIAN AND FORMALISM

We first construct the tight-binding Hamiltonian of ferromagnetic graphene in the presence of exchange field M and external magnetic field B [37]:

$$H = \sum_{i,\sigma}(\varepsilon_i - \sigma_z M)c^\dagger_{i\sigma}c_{i\sigma} - \sum_{\langle i,j\rangle,\sigma} t e^{i\phi_{ij}}c^\dagger_{i\sigma}c_{j\sigma}, \qquad (1)$$

where $c^\dagger_{i\sigma}$ and $c_{i\sigma}$ are the creation and annihilation operators at the discrete site i. $\varepsilon_i = E_0 + w_i$ stands for the on-site energy, where E_0 is the Dirac-point energy, and we set $E_0 = 0$ in the following calculations. w_i is the on-site disorder energy, which exists only in the central scattering region denoted by the black rectangles in the top sketches of Fig. 2. The disorder

w_i distributes uniformly in the range of $[-W/2, W/2]$, in which W is the disorder strength. t is the nearest-neighbor hopping energy. A phase factor $\phi_{ij} = \int_i^j \vec{A} \cdot d\vec{l}/\phi_0$ is considered in the hopping item when a perpendicular magnetic field is applied on ferromagnetic graphene. Here $\vec{A} = (-By, 0, 0)$ is the magnetic vector potential, and $\phi_0 = \hbar/e$ is the magnetic-flux quantum.

Without SOI, the spin is conserved, i.e., $[\hat{s}_z, \hat{H}] = 0$, and then all the physical quantities related to spin up (down) can be calculated in spin-up (down) subspace. The current in lead α with spin σ is calculated by using the Landauer-Büttiker formula

$$J_{\alpha\sigma} = \frac{1}{h} \sum_{\beta} \int T_{\alpha\beta,\sigma}(f_\alpha - f_\beta) dE, \tag{2}$$

where $T_{\alpha\beta,\sigma} = \mathrm{Tr}[\mathbf{\Gamma}_{\alpha\sigma} \mathbf{G}^{\mathrm{r}}_{\sigma} \mathbf{\Gamma}_{\beta\sigma} \mathbf{G}^{\mathrm{a}}_{\sigma}]$ [39–41] is the transmission coefficient of spin σ from lead β to α. The linewidth function $\mathbf{\Gamma}_{\alpha\sigma} = i[\mathbf{\Sigma}^r_{\alpha\sigma} - \mathbf{\Sigma}^a_{\alpha\sigma}]$. The Green function $\mathbf{G}^r_\sigma = \mathbf{G}^{a,\dagger}_\sigma = [E\mathbf{I} - \mathbf{H}_{C,\sigma} - \sum_\alpha \mathbf{\Sigma}^r_{\alpha\sigma}]^{-1}$, where $\mathbf{\Sigma}^r_{\alpha\sigma}$ is the retarded self-energy of lead α [42,43], $\mathbf{H}_{C,\sigma}$ is the Hamiltonian of central scattering region, and $\mathbf{I}$ is the unitary matrix. Then the charge current $J_{\alpha e} = e(J_{\alpha\uparrow} + J_{\alpha\downarrow})$ and spin current $J_{\alpha s} = \frac{\hbar}{2}(J_{\alpha\uparrow} - J_{\alpha\downarrow})$ in lead α are expressed as

$$\begin{aligned} J_{\alpha e} &= \frac{e}{h} \sum_{\beta} \int (T_{\alpha\beta,\uparrow} + T_{\alpha\beta,\downarrow})(f_\alpha - f_\beta) dE, \\ J_{\alpha s} &= \frac{1}{4\pi} \sum_{\beta} \int (T_{\alpha\beta,\uparrow} - T_{\alpha\beta,\downarrow})(f_\alpha - f_\beta) dE, \end{aligned} \tag{3}$$

where

$$f_\alpha(E, \mu_\alpha, \mathcal{T}_\alpha) = \frac{1}{e^{(E-\mu_\alpha)/k_B\mathcal{T}_\alpha} + 1}$$

is the Fermi distribution function of lead α with temperature $\mathcal{T}_\alpha$ and spin-independent chemical potential $\mu_\alpha = E_F + eV_\alpha$. Here e is the electron charge and V_α is the external bias. In the following, we consider the low-temperature limit $\mathcal{T} \to 0$ and make a linear expansion of Fermi distribution function around the Fermi energy E_F and temperature $\mathcal{T}$,

$$\begin{aligned} f_\alpha &= f_0 + eV_\alpha \frac{\partial f_\alpha}{\partial \mu_\alpha}\bigg|_{V_\alpha=0, \mathcal{T}_\alpha=\mathcal{T}} + \Delta\mathcal{T}_\alpha \frac{\partial f_\alpha}{\partial \mathcal{T}_\alpha}\bigg|_{V_\alpha=0, \mathcal{T}_\alpha=\mathcal{T}} \\ &= f_0 + f_0(f_0 - 1)\left[\frac{eV_\alpha}{k_B\mathcal{T}} + (E - E_F)\frac{\Delta\mathcal{T}}{k_B\mathcal{T}^2}\right], \end{aligned} \tag{4}$$

where $f_0 = \frac{1}{e^{(E-E_F)/k_B\mathcal{T}}+1}$ is the Fermi distribution at zero bias and zero thermal gradient.

As illustrated in the top sketches of Fig. 2, we use the two- and four-terminal devices to measure S_c and S_s, N_c and N_s, respectively. The Seebeck-type coefficients S_c and S_s depict the bias and spin currents corresponding to the thermal gradient in the two-terminal device, respectively. A temperature gradient is added between leads 1 and 2 by setting $\mathcal{T}_1 = \mathcal{T} + \Delta\mathcal{T}/2$ and $\mathcal{T}_2 = \mathcal{T} - \Delta\mathcal{T}/2$. The current induced by the temperature gradient can be offset by the bias ΔV. Then the charge Seebeck coefficient is defined as $S_c = \Delta V/\Delta\mathcal{T}$, with bias $\Delta V = V_1 - V_2$. Therefore we can get

$$S_c = -\frac{1}{e\mathcal{T}} \frac{\int dE(E - E_F)T_{12} f_0(f_0 - 1)}{\int dE T_{12} f_0(f_0 - 1)}. \tag{5}$$

In ferromagnetic graphene, S_s can be a spin indicator of spin-polarized Landau levels. Considering spin bias cannot be detected in experiment, we use a closed boundary condition $V_1 = V_2 = 0$ and then the spin Seebeck coefficient is defined as $S_s = J_s/\Delta\mathcal{T}$, where $J_s = J_{1s} = -J_{2s}$, owing to the current conservation. Then we have

$$S_s = -\frac{1}{4\pi}\left(\int T^s_{12}\left[\frac{(E - E_F)}{k_B\mathcal{T}^2} f_0(f_0 - 1)\right] dE\right). \tag{6}$$

In Eqs. (5) and (6), we defined $T_{\alpha\beta} = T_{\alpha\beta,\uparrow} + T_{\alpha\beta,\downarrow}$ and $T^s_{\alpha\beta} = T_{\alpha\beta,\uparrow} - T_{\alpha\beta,\downarrow}$, which are also used in the following expressions of the charge and spin Nernst coefficients.

The Nernst-type coefficients N_c and N_s depict the transverse thermoelectric power and transverse spin current induced by a longitudinal thermal gradient, respectively. In the four-terminal device, we set $\mathcal{T}_1 = \mathcal{T} + \Delta\mathcal{T}/2$, $\mathcal{T}_3 = \mathcal{T} - \Delta\mathcal{T}/2$, $\mathcal{T}_2 = \mathcal{T}_4 = \mathcal{T}$, and $V_1 = V_3 = 0$. As a result, a temperature gradient is added between the longitudinal leads 1 and 3. By using the open boundary condition $J_{2e} = J_{4e} = 0$ and spatial inversion symmetry $T_{21} = T_{43}$, $T_{23} = T_{41}$, and $T_{24} = T_{42}$, we can obtain the transverse voltage $\Delta V_t = V_2 - V_4$. Therefore the charge Nernst coefficient $N_c = -\Delta V_t/\Delta\mathcal{T}$ is expressed as

$$N_c = \frac{1}{e\mathcal{T}} \frac{\int dE(E - E_F)(T_{23} - T_{21}) f_0(f_0 - 1)}{\int dE(T_{21} + T_{23} + 2T_{24}) f_0(f_0 - 1)}. \tag{7}$$

By using the closed boundary condition $V_2 = V_4 = 0$, we can obtain J_{2s} and J_{4s}. In addition, $J_{2s} = -J_{4s}$ due to the spatial inversion symmetry $T^s_{21} = T^s_{43}$ and $T^s_{23} = T^s_{41}$. Then the spin Nernst coefficient $N_s = J_{2s}/\Delta\mathcal{T}$ is expressed as

$$N_s = -\frac{1}{4\pi} \int \left(T^s_{23} - T^s_{21}\right)\left[\frac{(E - E_F)}{k_B\mathcal{T}^2} f_0(f_0 - 1)\right] dE. \tag{8}$$

In the above definitions of thermoelectric coefficients, we used different boundary conditions according to experimental measuring practice. For example, in the charge thermoelectric transport processes, we use the open boundary condition $J_\alpha = 0$. The measurement of voltage is more convenient in experiment. Therefore, S_c and N_c are defined as $S_c = \Delta V/\Delta\mathcal{T}$ and $N_c = -\Delta V_t/\Delta\mathcal{T}$, respectively. However, in the spin thermoelectric transport processes, the definition of spin bias is ambiguous, while the spin current is clearly defined, which can be detected in experiment. As a result, instead of $V_{\alpha s}$, with the closed boundary condition $V_\alpha = 0$, the spin current $J_{\alpha s}$ is used to define spin thermoelectric coefficients as $S_s = J_s/\Delta\mathcal{T}$ and $N_s = J_{2s}/\Delta\mathcal{T}$, respectively. In fact, if spin bias $V_{\alpha s}$ can be defined through $J_{\alpha s} = 0$, N_s would share a similar magnitude with N_c.

III. NUMERICAL RESULTS AND DISCUSSION

To understand the thermoelectric transport properties of a ferromagnetic graphene nanoribbon under a strong magnetic field, we first analyze the energy bands with exchange fields $M = 0.04t$ and $0.08t$ in Figs. 1(a) and 1(b), respectively. Due to the formation of Landau levels in the presence of a strong

magnetic field, the zigzag and armchair ribbons have the same nontrivial edge states. Here we only show the results of the zigzag ribbon. For graphene ribbon under a strong magnetic field, two sets of Landau levels are formed, and the filling factor $\nu_\sigma = \pm 1, \pm 3, \pm 5, \ldots$, where $\sigma = \uparrow$ and $\downarrow$ represent spin up and spin down, respectively. $\nu_\sigma > 0$ and $\nu_\sigma < 0$ denote the electron and hole filling, respectively. Therefore the chiralities of the edge states are opposite for $\nu_\sigma > 0$ and $\nu_\sigma < 0$, i.e., the Chern number $-C_e(E_F) = C_h(-E_F)$. At the Dirac point, the chirality of the edge state changes from clockwise to anticlockwise, and vice versa, i.e., $C_{e/h} = \pm 1 \rightarrow C_{e/h} = \mp 1$. When the exchange field M is considered, the Nth Landau level with spin σ is $E_{N,\sigma} = \mathrm{sgn}(N)\sqrt{2|N|}\hbar v_F l_B^{-1} + \sigma M$, where the Fermi velocity $v_F = 3at/2\hbar$, magnetic length $l_B = \sqrt{\hbar/eB}$. The spin-up and spin-down Dirac points shift to $\pm M$, respectively. Then the spin-up (the red solid lines) and spin-down (the black dashed lines) bands are separated from each other in the absence of SOI. This means the *CT*-QSH effect ($C_{e,\downarrow} = -C_{h,\uparrow}$) can be realized in ferromagnetic graphene [the cyan regions in Figs. 1(a) and 1(b)]. Different from the conventional QSH effect protected by the time-reversal symmetry with $C_\downarrow = -C_\uparrow$, the *CT*-QSH effect in ferromagnetic graphene is protected by the *CT* invariance, where C is the charge conjugation operation and T means the time-reversal symmetry. The corresponding edge states are presented in the right top panel of Fig. 1, in which a pair of edge states with opposite spin and conjugated charge, i.e., spin-up holes (the red hollow circle with $\uparrow$) and spin-down electrons (the black solid circle with $\downarrow$), propagate toward opposite directions.

With the increase of M, the zeroth Landau level $E_{N=0,\sigma} = \pm M$ exceeds nonzero Landau levels $E_{N\neq 0,\bar{\sigma}}$. Therefore the QSH and QH effects coexist with $C_{e/h,\uparrow} \neq -C_{h/e,\downarrow}$, namely, the QSH + QH region [the yellow region in Fig. 1(b)]. We present the corresponding edge states in the right middle panel, in which one spin-up hole (the red hollow circles with $\uparrow$) propagates anticlockwise with $C_{h,\uparrow} = -1$, and three spin-down electrons (the black solid circles with $\downarrow$) propagate clockwise with $C_{e,\downarrow} = 3$. Furthermore, the QH effect appears at the high-energy region $|E_F| > M$ [the white region in Figs. 1(a) and 1(b)]. In this region, the charge conjugation is fixed for spin-up and spin-down carriers, and the edge states of electrons or holes propagate with fixed chirality, clockwise or anticlockwise with $(C_{e,\uparrow} \neq C_{e,\downarrow}) > 0$ or $(C_{h,\uparrow} \neq C_{h,\downarrow}) < 0$. In the right bottom panel of Fig. 1, we show the edge states of the QH region in which three spin-up holes (the red hollow circles with $\uparrow$) and one spin-down hole (the black hollow circles with $\downarrow$) propagate anticlockwise, corresponding to $C_{h,\uparrow} = -3$ and $C_{h,\downarrow} = -1$, respectively. In summary, according to the filling factor ν_σ, the energy bands are divided into two regions (*CT*-QSH and QH) and three regions (*CT*-QSH, QSH + QH, and QH) under exchange fields $M = 0.04t$ and $0.08t$, respectively. Novel thermoelectric transport properties appear at Landau levels.

Next we use the thermoelectric coefficients S_c, S_s, N_c, and N_s to describe how Landau levels are filled up. Correspondingly, thermoelectric coefficients are distinguished as the QSH type and QH type at the zeroth and nonzero Landau levels, respectively. The QSH- and QH-type thermoelectric transport properties are solely determined by the helical and chiral edge states, respectively. In Figs. 2 and 3, we plot S_c, S_s, N_c, and N_s versus Fermi energy E_F under the exchange field $M = 0.04t$ and $0.08t$, respectively. For easy analysis, we copy the same energy bands in Figs. 1(a) and 1(b) to Figs. 2 and 3 as backgrounds, respectively. Correspondingly, comparing with Fig. 2, the QSH + QH region appears in Fig. 3. The Seebeck- and Nernst-type coefficients are measured in the two- and four-terminal devices, respectively. We can find a series of peaks at Landau levels. Along the black arrows, the temperatures for each curve are $k_B\mathcal{T} = 0.001t, 0.002t, 0.003t, 0.005t$. With the increase of $k_B\mathcal{T}$, the peak half-width of S_c, S_s, N_c, and N_s become wider because the Landau level expands at high temperature.

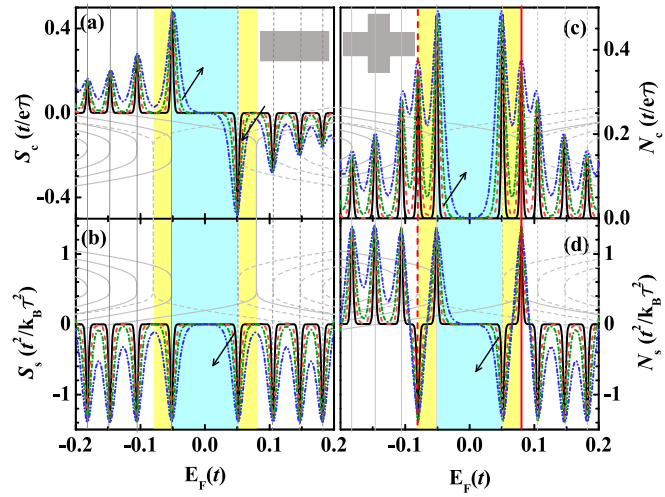

FIG. 3. Same as Fig. 2, except the exchange field $M = 0.08t$.

As shown in Figs. 2(a), 3(a), 2(b), and 3(b), we first focus on the Seebeck-type coefficients S_c and S_s calculated in the two-terminal device. The QSH-type S_c and S_s are zero when E_F crosses the zeroth Landau levels because the two-terminal device cannot feel the change of chirality from $C_{e/h} = \pm 1$ to $C_{e/h} = \mp 1$. However, the Seebeck-type coefficients can fell the change of filling factor at nonzero Landau levels $E_{N\neq 0,\sigma}$, where the filling factor $\nu = \nu_\uparrow + \nu_\downarrow$ changes by 2, but the chirality of edge states remain unchanged, leading to the nonzero values of the QH-type S_c and S_s. Therefore there is only the QH-type S_c and S_s at nonzero Landau levels $E_{N\neq 0,\sigma}$ (the vertical gray lines). For ferromagnetic graphene with the *CT*-QSH effect, $C_{e,\sigma}(E_F) = -C_{h,\bar{\sigma}}(-E_F)$. Then the following comparisons between S_c and S_s are clear: (i) The parity of S_c is opposite to S_s, i.e., S_c is an odd function of E_F while S_s is an even function. This is because S_c cannot feel the opposite chiralities of $C_{e,\sigma}(E_F)$ and $C_{h,\bar{\sigma}}(-E_F)$, but S_s can. (ii) S_c is always negative (positive) at Landau level $E_{N>0,\sigma}$ ($E_{N<0,\sigma}$), denoting the electron (hole) nature. The sign of S_s depends on the spin σ of Landau level $E_{N\neq 0,\sigma}$, denoting the spin nature. (iii) The peak height of S_c decreases as E_F increases, while the peak height of S_s remains unchanged due to the closed boundary condition used in the calculations of S_s.

As shown in Figs. 2(c), 3(c), 2(d), and 3(d), we next consider the Nernst-type coefficients N_c and N_s calculated in the four-terminal device. Comparing with S_c and S_s, we can find (i) in addition to the QH-type N_c and N_s at nonzero Landau

levels $E_{N\neq 0,\sigma}$ (the vertical gray lines), the QSH-type N_c and N_s appear at the zeroth Landau levels $E_{N=0,\sigma} = \pm M$ (the vertical red lines), which is different from the conventional QSH system, in which N_c and N_s are zero. (ii) Concerning the QH-type thermoelectric coefficients, $|N_c| = |S_c|$ and $|N_s| = |S_s|$. Their signs can be obtained by the CT invariance as follows. The signs of S_c for electrons and holes are opposite, and S_c is an odd function of E_F. However, we find N_c is electron-hole (e-h) independent. This is because in addition to the e-h symmetry, the four-terminal device can feel the opposite chiralities of electrons and holes. Considering $C_e = -C_h$ and $E_e = -E_h$, N_c is an even function of E_F. Similar to the Seebeck-type coefficients, the parities of N_c and N_s versus E_F are also opposite due to the CT invariance $C_{e,\sigma}(E_F) = -C_{h,\bar{\sigma}}(-E_F)$. Besides, the parities of S_s and N_s are also opposite. As shown in Figs. 2(c), 2(d), 3(c), and 3(d), N_c is always positive, while N_s can be positive or negative depending on the spin σ of Landau level $E_{N,\sigma}$. $N_s > 0$ and $N_s < 0$ correspond to the spin-up and spin-down Landau levels [the vertical solid and dashed lines in Figs. 2(d) and 3(d)], revealing the spin indicator feature of N_s.

Combining Figs. 2 and 3, the QSH + QH region appears when the zeroth Landau level $E_{N=0,\sigma} = \pm M$ exceeds nonzero Landau levels $E_{N\neq 0,\bar{\sigma}}$. The special fact of the QSH + QH region is the two types of boundaries: the QSH and QH types. Accordingly, the QSH- and QH-type thermoelectric coefficients appear at two boundaries of the QSH + QH region, as shown in Figs. 3(c) and 3(d). We note that although the QSH + QH region varies with M, there are only two types of thermoelectric coefficients (QSH and QH). Therefore we should be more concerned about the boundaries of topological regions in the calculations, from which we can judge which type of edge states is responsible for the thermoelectric coefficients, rather than the topological regions. In the presence of a strong magnetic field, the peak height of the QH-type thermoelectric coefficient remains unchanged under exchange fields $M = 0.04t$ and $0.08t$; only the peak position has a change. For the QSH-type thermoelectric coefficients, the peak height of the QSH-type N_c varies with M; the QSH-type N_s remains unchanged. Moreover, the peak positions of the QSH-type N_c and N_s vary with M. In summary, from Figs. 2 and 3, we have the QH-type $S_c = -\mathrm{sgn}(c)N_c$ and $S_s = \mathrm{sgn}(c)N_s$, where $\mathrm{sgn}(c)$ represents the sign of charge, which is $+1$ for the electron and -1 for the hole. N_c is positive and depends on the filling factor, while the sign of N_s depends on the spin of the Landau level, and its magnitude is independent of filling factor.

In the following, we quantitatively derive the rule of the peak height of S_c, S_s, N_c, and N_s. We focus on the boundaries of topological regions, from which we can judge the type (QSH or QH) of thermoelectric coefficients. For ferromagnetic graphene under a strong magnetic field, the transmission coefficients are quantized due to the formation of edge states. In the calculations, for simplicity we define

$$\begin{aligned}
\Delta T_{\alpha\beta,N,\sigma} &= T_{\alpha\beta,\sigma}(E_N^+) - T_{\alpha\beta,\sigma}(E_N^-) \\
T_{\alpha\beta,N} &= \sum_\sigma \frac{1}{2}[T_{\alpha\beta,\sigma}(E_N^+) + T_{\alpha\beta,\sigma}(E_N^-)], \\
\Delta T_{\alpha\beta,N} &= \sum_\sigma \Delta T_{\alpha\beta,N,\sigma} \\
&= \sum_\sigma [T_{\alpha\beta,\sigma}(E_N^+) - T_{\alpha\beta,\sigma}(E_N^-)], \\
\Delta T^s_{\alpha\beta,N} &= \sum_\sigma \sigma \Delta T_{\alpha\beta,N,\sigma} \\
&= \sum_\sigma \sigma [T_{\alpha\beta,\sigma}(E_N^+) - T_{\alpha\beta,\sigma}(E_N^-)], \qquad (9)
\end{aligned}$$

where $E_N^\pm = E_{N,\sigma} \pm 0^+$, $T_{\alpha\beta,N}$ is the mean transmission coefficient from lead β to α around Landau level $E_{N,\sigma}$, and $\Delta T_{\alpha\beta,N}$ and $\Delta T^s_{\alpha\beta,N}$ are the changes of charge and spin transmission coefficients, respectively. Then, using integrations $\int_0^{\pm\infty} \frac{dx}{(e^x+1)(e^{-x}+1)} = \pm\frac{1}{2}$ and $\int_0^{\pm\infty} \frac{xdx}{(e^x+1)(e^{-x}+1)} = \ln 2$, we can get analytic expressions of thermoelectric coefficients by integrating Eqs. (5)–(8). The peak heights of the Seebeck- and Nernst-type coefficients at Landau level $E_{N,\sigma}$ are expressed as

$$\begin{aligned}
-S_{c,N} &= \ln 2 \frac{\Delta T_{12,N}}{T_{12,N}} \frac{t}{e\mathcal{T}}, \\
S_{s,N} &= \ln 2 \Delta T^s_{12,N} \frac{t^2}{4\pi k_B \mathcal{T}^2}, \qquad (10)
\end{aligned}$$

and

$$\begin{aligned}
N_{c,N} &= \ln 2 \frac{\Delta T_{23,N} - \Delta T_{21,N}}{T_{23,N} + T_{21,N}} \frac{t}{e\mathcal{T}}, \\
N_{s,N} &= \ln 2 (\Delta T^s_{23,N} - \Delta T^s_{21,N}) \frac{t^2}{4\pi k_B \mathcal{T}^2}. \qquad (11)
\end{aligned}$$

As discussed above, thermoelectric coefficients are divided into the QSH and QH types at the zeroth and nonzero Landau levels, respectively. First, we use $E_n^{\mathrm{QH}} = E_{N\neq 0,\sigma}$ to define the position of the nth peak of the QH-type thermoelectric coefficient. Here n tells only which peak is referred to; it is not usually equivalent to the N and not related to the σ of Landau level $E_{N\neq 0,\sigma}$. In other words, the nth peak may come from any nonzero Landau level $E_{N\neq 0,\sigma}$. On the other hand, the QSH-type thermoelectric coefficients appear at the zeroth Landau levels $E_{N=0,\sigma} = \pm M$, and the peak position varies with M. We use $E_m^{\mathrm{QSH}} = E_{N=0,\sigma}$ to define the position of the mth peak of the QSH-type thermoelectric coefficient under different M, where m is the sequence number. In addition, we define $n > 0$ and $m > 0$ for $E_F > 0$, $n < 0$ and $m < 0$ for $E_F < 0$.

We first derive the QH-type thermoelectric coefficients that appear at nonzero Landau levels with energy $E_n^{\mathrm{QH}} = E_{N\neq 0,\sigma}$. The Seebeck-type thermoelectric coefficients are measured in the two-terminal devices. Considering $E_F > 0$, the QH-type S_c and S_s appear at the nonzero Landau level $E_{N>0,\sigma}$. From Eq. (10), the nth peak heights of the QH-type S_c and S_s are expressed as

$$\begin{aligned}
-S_{c,n}^{\mathrm{QH}} &= \ln 2 \frac{\Delta T_{12,n}}{T_{12,n}} \frac{t}{e\mathcal{T}}, \\
S_{s,n}^{\mathrm{QH}} &= \ln 2 \Delta T^s_{12,n} \frac{t^2}{4\pi k_B \mathcal{T}^2}, \qquad (12)
\end{aligned}$$

where $T_{12,n}$ is the mean transmission coefficient from lead 2 to lead 1 at $E_n^{\mathrm{QH}} = E_{N>0,\sigma}$, and $\Delta T_{\alpha\beta,n}$ and $\Delta T^s_{\alpha\beta,n}$ are the

changes of charge and spin transmission coefficients, respectively. For the two-terminal device, $T_{12,\sigma} = \nu_\sigma = 1, 3, 5, ...$ in the QH region. When E_F crosses the spin-up (spin-down) Landau level $E_{N>0,\uparrow(\downarrow)}$, the value of $\nu_\uparrow$ ($\nu_\downarrow$) changes by 2, and $\nu_\downarrow$ ($\nu_\uparrow$) remains unchanged. Consequently, we have $\Delta T_{12,n} = \Delta T_{12,n,\uparrow(\downarrow)} = 2$ regardless of spin. In addition, we find $T_{12,n} = 2n + 1$ due to the zeroth Landau level, and $\Delta T^s_{12,n} = \mathrm{sgn}(s)2$ at Landau levels $E_{N>0,\sigma}$, where $\mathrm{sgn}(s)$ denotes the sign of spin, which is $+1$ for spin up $\uparrow$ and -1 for spin down $\downarrow$. As a result, for $E_F > 0$, $S^{\mathrm{QH}}_{c,n} = -\ln 2/(n + 1/2)$ and $S^{\mathrm{QH}}_{s,n} = \mathrm{sgn}(s)2\ln 2$ with $n = (\nu_\uparrow + \nu_\downarrow)/2 - 1$. Then, according to the *CT* invariance, the equations of the QH-type S_c and S_s at $E_F < 0$ can be easily obtained. Therefore, the QH-type Seebeck coefficients at Landau level $E^{\mathrm{QH}}_n = E_{N\neq 0,\sigma}$ are expressed as

$$S^{\mathrm{QH}}_{c,n} = -\mathrm{sgn}(c)\ln 2/(|n| + 1/2)\,\frac{t}{e\mathcal{T}},$$
$$S^{\mathrm{QH}}_{s,n} = \mathrm{sgn}(c)\mathrm{sgn}(s)2\ln 2\,\frac{t^2}{4\pi k_B \mathcal{T}^2}. \tag{13}$$

The peak height of the QH-type S_c depends on filling factor, while the magnitude of the QH-type S_s is independent of filling factor.

The QH-type Nernst coefficients appear at nonzero Landau levels $E_{N\neq 0,\sigma}$. Considering $E_F > 0$, the QH-type N_c and N_s appear at the nonzero Landau level $E_{N>0,\sigma}$; the edge states contributed by electrons correspond to the quantized $T_{23,N}$. Besides, $T_{21,\downarrow} = 0$; $T_{21,\uparrow}$ does not change at nonzero Landau level $E_{N>0,\sigma}$. This means, around $E_F = E_{N>0,\sigma}$, $\Delta T_{21,N} = 0$, $\Delta T^s_{21,N} = 0$, and only the mean transmission coefficient $T_{21,N} \neq 0$. As a result, the nth peak heights of the QH-type N_c and N_s are expressed as

$$N^{\mathrm{QH}}_{c,n} = \ln 2\,\frac{\Delta T_{23,n}}{T_{23,n} + T_{21,n}}\,\frac{t}{e\mathcal{T}},$$
$$N^{\mathrm{QH}}_{s,n} = \ln 2\,\Delta T^s_{23,n}\,\frac{t^2}{4\pi k_B \mathcal{T}^2}, \tag{14}$$

where $T_{23,n}$ is the mean transmission coefficient from lead 3 to 2 at $E^{\mathrm{QH}}_n = E_{N>0,\sigma}$, and $\Delta T_{23,n}$ and $\Delta T^s_{23,n}$ are the changes of charge and spin transmission coefficients, respectively. Due to the topological edge states, $T^{(4)}_{21,\sigma} + T^{(4)}_{23,\sigma}$ in the four-terminal device is the same as $T^{(2)}_{12,\sigma}$ in the two-terminal device for all Landau levels; thus $T_{23,n} + T_{21,n} = 2n + 1$. Moreover, $\Delta T_{23,n} = \Delta T_{23,n,\uparrow(\downarrow)} = 2$ and $\Delta T^s_{23,n} = \mathrm{sgn}(s)2$ at nonzero Landau level $E_{N>0,\sigma}$. As a result, for $E_F > 0$, $N^{\mathrm{QH}}_{c,n} = |S^{\mathrm{QH}}_{c,n}| = \ln 2/(n + 1/2)$ and $N^{\mathrm{QH}}_{s,n} = \mathrm{sgn}(s)2\ln 2$ with $n = (\nu_\uparrow + \nu_\downarrow)/2 - 1$. Then, according to the *CT* invariance, the equations of the QH-type N_c and N_s at $E_F < 0$ can be easily obtained. Therefore, the QH-type Nernst coefficients at $E^{\mathrm{QH}}_n = E_{N\neq 0,\sigma}$ are expressed as

$$N^{\mathrm{QH}}_{c,n} = \ln 2/(|n| + 1/2)\,\frac{t}{e\mathcal{T}},$$
$$N^{\mathrm{QH}}_{s,n} = \mathrm{sgn}(s)2\ln 2\,\frac{t^2}{4\pi k_B \mathcal{T}^2}. \tag{15}$$

The nth peak heights QH-type N_c and S_c are inverse to $|n| + 1/2$, denoting the half-integer QH effect. The signs of the QH-type N_s and S_s depend on the spin σ of Landau level $E_{N\neq 0,\sigma}$, and their magnitudes are independent of filling factor.

We next derive the QSH-type thermoelectric coefficients that appear at the zeroth Landau levels $E_{N=0,\sigma}$. At the boundary between the *CT*-QSH (QSH + QH) and QH regions for $M = 0.04t$ ($0.08t$), the filling factor changes from $\nu_\sigma = \pm 1$ to $\nu_\sigma = \mp 1$ due to the helical edge states. Because the two-terminal device cannot feel the change of chirality of the edge state, the QSH-type Seebeck coefficients at $E^{\mathrm{QSH}}_m = E_{N=0,\sigma}$ are expressed as

$$S^{\mathrm{QSH}}_{c,m} = 0, \quad S^{\mathrm{QSH}}_{s,m} = 0. \tag{16}$$

In the conventional QSH system, the S_c and S_s are also zero, but the physics are different. The thermoelectric signal is sensitive to the details of the density of states. However, because of the single-band-gap structure in the conventional QSH system, the information about the bulk density of states is missing, and the transmission $T_{\alpha\beta}$ and $T^s_{\alpha\beta}$ remain constant for all the E_F in the energy gap. As a result, not only S_c and S_s, but also N_c and N_s are zero in the conventional QSH system.

From Eq. (11), we derive the expressions of peak heights of the QSH-type N_c and N_s, which appear at $E_{N=0,\sigma} = \pm M$. Considering $E_F > 0$, the QSH-type N_c and N_s appear at the zeroth Landau level $E_{N=0,\uparrow} = M$. The chirality of spin-up edge state changes from clockwise to anticlockwise ($C_{e,\uparrow} = 1$ to $C_{h,\uparrow} = -1$). The change of chirality is revealable in the four-terminal devices through $T_{21,\uparrow}$ and $T_{23,\uparrow}$. Around $E_F = M$, only the spin-up transmission coefficients have a change. As a result, the mth peak heights of the QSH-type N_c and N_s are expressed as

$$N^{\mathrm{QSH}}_{c,m} = \ln 2\,\frac{\Delta T_{23,m,\uparrow} - \Delta T_{21,m,\uparrow}}{T_{23,m} + T_{21,m}}\,\frac{t}{e\mathcal{T}},$$
$$N^{\mathrm{QSH}}_{s,m} = \ln 2(\Delta T_{23,m,\uparrow} - \Delta T_{21,m,\uparrow})\,\frac{t^2}{4\pi k_B \mathcal{T}^2}. \tag{17}$$

where $\Delta T_{23,m,\uparrow}$ and $T_{23,m}$ are the changes of spin up and the mean transmission coefficients from lead 3 to 2 at $E^{\mathrm{QSH}}_m = E_{N=0,\uparrow}$, respectively, and so are the $\Delta T_{21,m,\uparrow}$ and $T_{21,m}$ from lead 1 to 2. Apparently, at around $E_F = M$, $T_{21,\uparrow} = 1$ changes to $T_{23,\uparrow} = 1$ owing to the change of chirality of the spin-up edge state. $\Delta T_{23,m,\uparrow} - \Delta T_{21,m,\uparrow} = 1 - (-1) = 2$ is always satisfied, and $T_{21,m} + T_{23,m} = 2m$. Subsequently, with the increase of M, $N^{\mathrm{QSH}}_{c,m} = \ln 2/m$ and $N^{\mathrm{QSH}}_{s,m} = 2\ln 2$ at $E_{N=0,\uparrow}$, where $m = (\nu_\uparrow + \nu_\downarrow)/2$ is the total filling factor at $E_F = E^+_{N=0,\uparrow}$ [the vertical red solid lines in Figs. 2(c), 3(c), 2(d), and 3(d)]. Then, based on the *CT* invariance, the equations of the QSH-type N_c and N_s at $E_F < 0$ can be easily obtained. Therefore, the QSH-type Nernst coefficients at $E^{\mathrm{QSH}}_m = E_{N=0,\sigma}$ are expressed as

$$N^{\mathrm{QSH}}_{c,m} = \frac{\ln 2}{|m|}\,\frac{t}{e\mathcal{T}},$$
$$N^{\mathrm{QSH}}_{s,n} = \mathrm{sgn}(s)2\ln 2\,\frac{t^2}{4\pi k_B \mathcal{T}^2}. \tag{18}$$

The mth peak heights of the QSH-type N_c are inverse to $|m|$, denoting the integer QH effect, which is different from the QH-type N_c. The peak height of the QSH-type N_s is always $2\ln 2$, and its sign depends on the spin of $E_{N=0,\sigma}$, which is the same as the QH-type N_s.

To compare the thermoelectric transport properties of different topological regimes, we summarize the QH-type,

TABLE I. The magnitude of thermoelectric coefficients for different topological regimes. sgn(c) represents the sign of charge, which is $+1$ for the electron and -1 for the hole. In addition, sgn(s) denotes the sign of spin, which is $+1$ for spin up $\uparrow$ and -1 for spin down $\downarrow$.

	QH type	QSH type	Conventional QSH type
Charge	$S_{c,n}^{\mathrm{QH}} = -\mathrm{sgn}(c)\ln 2/(\lvert n\rvert + \frac{1}{2})$ $N_{c,n}^{\mathrm{QH}} = \ln 2/(\lvert n\rvert + \frac{1}{2})$	$S_{c,m}^{\mathrm{QSH}} = 0$ $N_{c,m}^{\mathrm{QSH}} = \ln 2/\lvert m\rvert$	$S_c = 0$ $N_c = 0$
Spin	$S_{s,n}^{\mathrm{QH}} = \mathrm{sgn}(s)\mathrm{sgn}(c)2\ln 2$ $N_{s,n}^{\mathrm{QH}} = \mathrm{sgn}(s)2\ln 2$	$S_{s,m}^{\mathrm{QSH}} = 0$ $N_{s,m}^{\mathrm{QSH}} = \mathrm{sgn}(s)2\ln 2$	$S_s = 0$ $N_s = 0$

QSH-type, and conventional QSH-type thermoelectric coefficients in Table I, from which one can clearly see the differences between ferromagnetic graphene with the *CT*-QSH effect and conventional QSH system. In the conventional QSH system, both the Seebeck and Nernst coefficients are zero because the information about the bulk density of states is missing within the nontrivial single band gap. By contrast, benefiting from the multi-band-gap structure of ferromagnetic graphene with the *CT*-QSH effect, the Nernst-type coefficients accurately record the details of the band structure. As shown in Table I, the QH-type N_c is obviously distinguished from the QSH-type N_c, although both of them are dependent on filling factor. Therefore we can distinguish the category of Landau levels (the QSH- and QH-type) by the magnitude of N_c. As for N_s, because the offset voltage in the detecting terminals is zero, the spin thermoelectric coefficient keeps a maximum value of $2\ln 2$. In addition, the sign of N_s is dependent on the spin of the Landau level, revealing the spin indicator feature of the spin thermoelectric coefficients. It can be seen that $N_s > 0$ at $E_{N=0,\uparrow} = M$ and $N_s < 0$ at $E_{N=0,\downarrow} = -M$ are always true regardless of exchange field M. The boundary between the *CT*-QSH (QSH + QH) and QH regions is $E_{N=0,\sigma} = |M|$. Therefore the sign of N_s at the zeroth Landau level is the point where one could make predictions for experiments.

Through the above analysis, it is clear that the spin thermoelectric coefficients have the constant magnitude, i.e., $|S_s| = |N_s| = 2\ln 2$, while the magnitude of S_c or N_c depends on the total filling factor $\nu = \nu_\uparrow + \nu_\downarrow$. Next, to manifest the rules of peak heights of S_c and N_c, we plot S_c and N_c versus E_F under different strong magnetic fields $\phi = 0.005$, 0.008, and 0.010 with $M = 0.04t$ and different exchange fields $M = 0.02t$, $0.04t$, $0.07t$, and $0.10t$ with $\phi = 0.005$ in Fig. 4. In Figs. 4(a) and 4(c), the backgrounds are the energy bands of $\phi = 0.005$ and 0.010, respectively. The Landau levels are consistent with the positions of peaks (the vertical black and blue lines). So are the backgrounds in Figs. 4(b) and 4(d) for $M = 0.02t$ and $0.10t$, respectively. As shown in Figs. 4(a) and 4(c), the first peaks of the QH-type S_c and N_c shift outwards because the nonzero Landau level $E_{N\neq 0,\sigma}$ increases with the increase of ϕ. However, as shown in Figs. 4(b) and 4(d), with the increase of M, the first peaks of the QH-type S_c and N_c shift inwards because the nonzero Landau levels $E_{N>0,\downarrow}$ and $E_{N<0,\uparrow}$ shift M towards $E_F = 0$ in the presence of M. The nth peak heights of the QH-type $|S_c|$ and N_c satisfy $S_{c,n} = -\mathrm{sgn}(c)\ln 2/(|n| + \frac{1}{2})$ and $N_{c,n} = \ln 2/(|n| + \frac{1}{2})$ for $|n| = 1, 2, 3, \ldots$. Here, n is not usually equivalent to the N and not related to the spin σ of Landau level $E_{N\neq 0,\sigma}$. As an example, for $\phi = 0.005$ in Fig. 4(a) and $M = 0.02t$ in Fig. 4(b) (the black lines), the third and second peaks of S_c appear at the first Landau level $E_{N=-1,\uparrow}$ [the vertical red lines in Figs. 4(a) and 4(b)]; however, it does not interfere its height rule of $-\mathrm{sgn}(c)\ln 2/(|n| + 1/2)$. In addition to the QH-type S_c and N_c, there is also the QSH-type N_c located at $E_{N=0,\uparrow} = M$. In Fig. 4(c), fixing M, all the peaks of the QSH-type N_c locate at $E_F = 0.04t$ regardless of ϕ, and the peak heights remain unchanged [see the horizontal red line in Fig. 4(c)]. In Fig. 4(d), the QSH-type N_c for $M = 0.02t$ and $0.04t$ share the same peak height. However, with the further increase of M, the zeroth Landau level $E_{N=0,\uparrow}$ exceeds $E_{N>0,\downarrow}$. For $M = 0.02t$ ($0.04t$), $0.07t$, and $0.10t$, the QSH-type N_c appears at $E_{N=0,\uparrow}$ with different peak heights, corresponding to the first, second, and third peaks [see the three horizontal red lines in Fig. 4(d)]. The peak height of the QSH-type N_c varies with exchange field and satisfies $N_{c,m} = \ln 2/|m|$ for $|m| = 1, 2, 3, \ldots$.

To intuitively distinguish the topological category, we plot the inverse of peak height of N_c and S_c (N_c^{-1} and S_c^{-1}) versus the sequence number of peak (n or m) in Figs. 5(a) and 5(b), respectively. Also, the S_c^{-1} for the integer QH effect is plotted for the convenience of comparing and analyzing. Several characters are summarized: (i) Considering the *CT* invariance and *e*-*h* symmetry, N_c is an even function of E_F, while S_c is an odd function. (ii) Thermoelectric transport contributed by the nonzero Landau level can be characterized by both the QH-type N_c and S_c. (iii) Thermoelectric transport contributed by the zeroth Landau level can be characterized only by the QSH-type N_c. (iv) The inverse of the nth peak heights of the

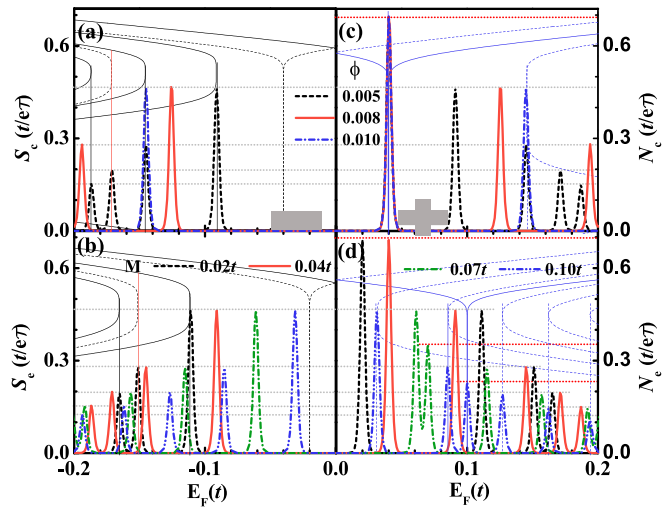

FIG. 4. (a) S_c and (c) N_c vs E_F under different strong magnetic fields ϕ for $M = 0.04t$. (b) S_c and (d) N_c vs E_F under different M for $\phi = 0.005$. The other parameters are temperature $k_B\mathcal{T} = 0.001t$, scattering width $N = 40$, and length $L = 40$.

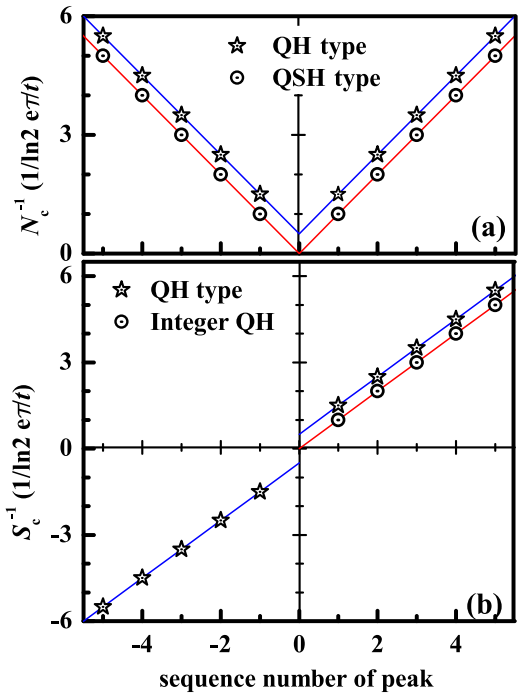

FIG. 5. N_c^{-1} and S_c^{-1} vs the sequence number of peak (n or m).

QH-type thermoelectric coefficients satisfy $N_{c,n}^{-1} = |S_{c,n}^{-1}| = (|n| + 1/2)/\ln 2$ [pentacles in Figs. 5(a) and 5(b)], which indicates the half-integer QH effect. (v) The inverse of the mth peak height of the QSH-type $N_{c,m}^{-1} = |m|/\ln 2$ [circles in Fig. 5(a)], similar to the integer QH effect [circles in Fig. 5(b)].

To compare with the results of a strong magnetic field, we plot S_c, S_s, N_c, and N_s versus E_F under weak magnetic fields $\phi = 0.0001$, 0.0003, 0.0005, and 0.0007 in Fig. 6. The background is the energy bands of zigzag ribbon with $\phi = 0.0003$. As thermoelectric transport reflects the details

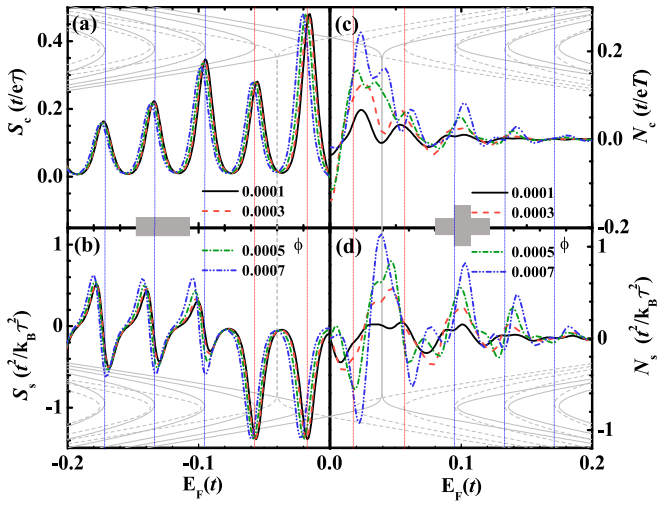

FIG. 6. (a–d) S_c, S_s, N_c, and N_s vs E_F under different weak magnetic fields ϕ. The other parameters are exchange field $M = 0.04t$, temperature $k_B\mathcal{T} = 0.003t$, scattering width $N = 40$, and length $L = 40$.

of the density of states, the peaks of S_c and S_s appear at the positions of every subband, as shown in Figs. 6(a) and 6(b). Here, we only show the results of the zigzag ribbon. It can be expected that the positions of S_c and S_s of the armchair ribbon are also consistent with its subbands. In the case of a weak magnetic field, Landau levels have not yet formed and all subbands are overlapped with each other. Consequently, the peak half-width of S_c and S_s expand seriously, and the peak heights distribute randomly with n. Because the conductance increases as E_F increases, S_c is always positive (negative) when $E_F < 0$ ($E_F > 0$). On the other hand, the sign of S_s is determined by the spin σ of the subband. The pure spin-up subband [the vertical red lines in Fig. 6(b)] contributes the negative (negative) S_s when $E_F < 0$ ($E_F > 0$). For the mixed spin subband [the vertical blue lines in Fig. 6(b)], the sign of S_s changes when E_F crosses the bottom of subbands. In the presence of a weak magnetic field, the Lorentz force is weak. The larger the Fermi energy E_F, the weaker the Lorentz force. Therefore the transverse deflection in the four-terminal devices is small in the weak magnetic field, and it becomes smaller with the increase of E_F. Comparing with the values of S_c and S_s, N_c and N_s in Figs. 6(c) and 6(d) are much smaller, especially for the large E_F. It is substantially different from the case of a strong magnetic field. Moreover, N_c and N_s are detected in the four-terminal device where both zigzag and armchair ribbons are involved. As a result, the peaks of N_c and N_s cannot coincide with the subband of the zigzag ribbon, especially at high Fermi energy, because Landau levels start to form at the Dirac point. Figures 6(c) and 6(d) clearly indicate the discrepancy of band structures of the zigzag and armchair ribbons.

Finally, we study the role of disorders on the thermoelectric transport of ferromagnetic graphene under a strong magnetic field. Under different exchange fields, the energy bands of ferromagnetic graphene can be divided into two regions (*CT*-QSH and QH) or three regions (*CT*-QSH, QSH + QH, and QH). Although the QSH + QH region varies with M, the QSH- and QH-type thermoelectric transport properties are determined by the helical and chiral edge states, as in the pure *CT*-QSH and QH regimes. Therefore, in the case of disorders, we only study the case of $M = 0.04t$ (QH and *CT*-QSH). Figure 7 shows the S_c, S_s, N_c, and N_s versus Fermi energy E_F with disorder strength $W = 0.0t$, $0.5t$, $1.0t$, and $2.0t$. The disorder is considered only in the central scattering region. All the curves are averaged over 500 random configurations, which is enough to obtain reasonable results. We also plot the energy bands as backgrounds for the convenience of analysis. As in a clean system, thermoelectric coefficients appear only when E_F crosses the Landau level $E_{N,\sigma}$. The magnitudes of the QH-type N_c and S_c depend on the sequence number of peaks, and so does the QSH-type N_c. The signs of the QH-type N_s and S_s are determined by the spin of the Landau level, and so is the QSH-type N_s.

We first study the influence of disorders on the QH-type thermoelectric coefficients. When disorder is not very strong, such as $W < 1.0t$, the sequentially arranged peaks are almost unchanged. When $W > 1.0t$, Landau levels are destroyed, and the peaks of thermoelectric coefficient are broken. The peak heights of S_c remain fairly stable, while the peak heights of N_c reduce significantly [Figs. 7(a) and 7(c)]. This means the

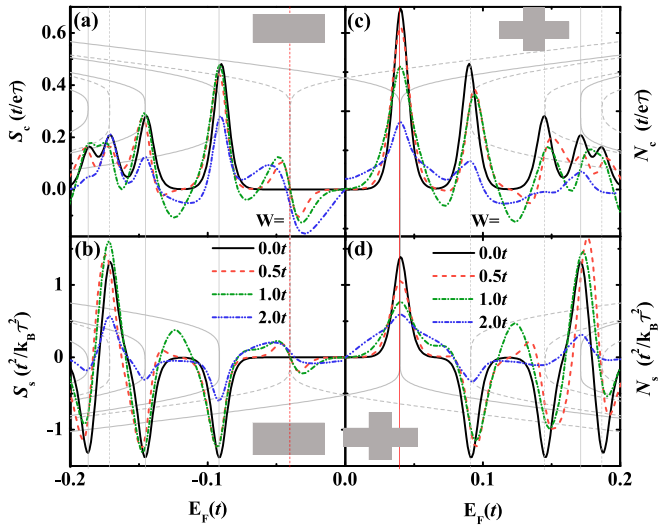

FIG. 7. (a–d) S_c, S_s, N_c, and N_s vs E_F under different disorder strengths W. The other parameters are $M = 0.04t$, $\phi = 0.005$, $k_B\mathcal{T} = 0.001t$, $N = 40$, and $L = 40$. All the curves are averaged over 500 random configurations.

QH-type S_c are more robust than the QH-type N_c because the four-terminal device is more sensitive to the backscattering induced by the disorders. With regard to the QH-type S_s and N_s, as long as the spins of Landau levels are uniform, S_s and N_s might be as robust as S_c and N_c [the negative S_s and N_s in Figs. 7(b) and 7(d)]. When the Landau level with different spin is involved, the robustness of S_s and N_s would be substantially weakened because of the spin offset from the broken edge states [positive S_s in Figs. 7(b)].

As for the QSH-type thermoelectric coefficients, both N_c and N_s appear at the zeroth Landau level $E_F = E_{N=0,\uparrow}$ [the vertical red lines in Figs. 7(c) and 7(d)] and decrease with the increase of W. As analyzed above, thermoelectric transport properties are solely determined by Landau level and the corresponding edge states. The helical edge states are robust only in the presence of spin-conserved disorders, while the chiral edge states can resist all kinds of disorders. Therefore, comparing with the QH-type thermoelectric coefficients, the QSH-type N_c and N_s decrease more rapidly than the QH-type N_c and N_s, indicating the QSH-type thermoelectric coefficients are more fragile. In addition, the QSH-type S_c and S_s are zero in clean systems because the longitudinal signal cannot feel the change of chirality of pure helical edge states around the zeroth Landau level. However, in the presence of disorders, the helical edge states are destroyed at $E_F = E_{N=0,\uparrow}$, and the transmission coefficients are not quantized anymore, which can be successfully captured by the longitudinal S_e and S_s as shown in Figs. 7(a) and 7(b). The sine like curves around $E_F = E_{N=0,\uparrow}$ indicate the helical nature of the QSH effect.

IV. CONCLUSION

In conclusion, based on the nonequilibrium Green's function and Landauer-Büttiker formula, we systematically investigated thermoelectric transport properties of ferromagnetic graphene under a strong magnetic field. The energy bands of ferromagnetic graphene were divided into the *CT*-QSH, QSH + QH, and QH regions according to the filling factor ν_σ. We used Seebeck coefficients (S_c and S_s) and Nernst coefficients (N_c and N_s) to describe the longitudinal and transverse (charge and spin) thermoelectric transport, respectively. The QSH-type thermoelectric coefficient appears at the zeroth Landau level, where the Chern number changes from $C_{\uparrow(\downarrow)} = \pm 1$ to $C_{\uparrow(\downarrow)} = \mp 1$. Because the two-terminal device cannot feel the change of chirality of the edge state, the QSH-type S_c and S_s are zero and only the QSH-type N_c and N_s were considered. By contrast, thermoelectric coefficients are all zero in the conventional QSH system. The QH-type thermoelectric coefficient appears at nonzero Landau level, across which the number of chiral edge states was changed. For the charge thermoelectric coefficients, the nth peak heights of the QH-type S_c and N_c satisfy $S_{c,n} = -\mathrm{sgn}(c)\ln 2/(|n| + \frac{1}{2})$ and $N_{c,n} = \ln 2/(|n| + \frac{1}{2})$, corresponding to the half-integer QH effect, while the mth peak height of the QSH-type N_c satisfies $N_{c,m} = \ln 2/|m|$, similar to the integer QH effect. Therefore we can distinguish the category of Landau levels (QH and QSH types) by the magnitude of N_c. On the other hand, for the spin thermoelectric transport, the magnitudes of S_s and N_s remain a constant $2\ln 2$, but their signs indicate the spin-polarization of Landau level. In the presence of disorders, the helical edge states were broken, which was confirmed by nonzero values of the QSH-type S_c and S_s. As a whole, the QH-type thermoelectric coefficients are more robust than those of the QSH type, because the chiral edge states are more robust. The QH-type S_c and S_s are more robust than the QH-type N_c and N_s because the four-terminal device is more sensitive to the backscattering.

ACKNOWLEDGMENT

This work was supported by NSF China under Grants No. 11674024 (Y.X.) and No. 11774238 (B.W.).

[1] G. E. W. Bauer, E. Saitoh, and B. J. van Wees, Spin caloritronics, Nat. Mater. **11**, 391 (2012).

[2] K. Behnia, M.-A. Méasson, and Y. Kopelevich, Oscillating Nernst-Ettingshausen Effect in Bismuth Across the Quantum Limit, Phys. Rev. Lett. **98**, 166602 (2007).

[3] A. S. Dzurak, C. G. Smith, C. H. W. Barnes, M. Pepper, L. Martín-Moreno, C. T. Liang, D. A. Ritchie, and G. A. C. Jones, Thermoelectric signature of the excitation spectrum of a quantum dot, Phys. Rev. B **55**, R10197 (1997).

[4] R. Scheibner, M. König, D. Reuter, A. D. Wieck, C. Gould, H. Buhmann, and L. W. Molenkamp, Quantum dot as thermal rectifier, New J. Phys. **10**, 083016 (2008).

[5] R. Bel, K. Behnia, Y. Nakajima, K. Izawa, Y. Matsuda, H. Shishido, R. Settai, and Y. Onuki, Giant Nernst Effect in $CeCoIn_5$, Phys. Rev. Lett. **92**, 217002 (2004).

[6] J. Chang, R. Daou, C. Proust, D. LeBoeuf, N. Doiron-Leyraud, F. Laliberté, B. Pingault, B. J. Ramshaw, R. Liang, D. A. Bonn, W. N. Hardy, H. Takagi, A. B. Antunes, I. Sheikin, K. Behnia, and L. Taillefer, Nernst and Seebeck Coefficients of the Cuprate Superconductor $YBa_2Cu_3O_{6.67}$: A Study of Fermi Surface Reconstruction, Phys. Rev. Lett. **104**, 057005 (2010).

[7] A. A. Balandin, Thermal properties of graphene and nanostructured carbon materials, Nat. Mater. **10**, 569 (2011).

[8] Y. Dubi and M. Di Ventra, Colloquium: Heat flow and thermoelectricity in atomic and molecular junctions, Rev. Mod. Phys. **83**, 131 (2011).

[9] K. Uchida, S. Takahashi, K. Harii, J. Ieda, W. Koshibae, K. Ando, S. Maekawa, and E. Saitoh, Observation of the spin Seebeck effect, Nature (London) **455**, 778 (2008).

[10] K. Uchida, J. Xiao, H. Adachi, J. Ohe, S. Takahashi, J. Ieda, T. Ota, Y. Kajiwara, H. Umezawa, H. Kawai, G. E. W. Bauer, S. Maekawa, and E. Saitoh, Spin Seebeck insulator, Nat. Mater. **9**, 894 (2010).

[11] C. M. Jaworski, J. Yang, S. Mack, D. D. Awschalom, J. P. Heremans, and R. C. Myers, Observation of the spin-Seebeck effect in a ferromagnetic semiconductor, Nat. Mater. **9**, 898 (2010).

[12] S. Meyer, Y.-T. Chen, S. Wimmer, M. Althammer, T. Wimmer, R. Schlitz, S. Geprägs, H. Huebl, D. Ködderitzsch, H. Ebert, G. E. W. Bauer, R. Gross, and S. T. B. Goennenwein, Observation of the spin Nernst effect, Nat. Mater. **16**, 977 (2017).

[13] P. Sheng, Y. Sakuraba, Y.-C. Lau, S. Takahashi, S. Mitani, and M. Hayashi, The spin Nernst effect in tungsten, Sci. Adv. **3** (2017).

[14] C. Jia and J. Berakdar, Anisotropic thermoelectric effect in helimagnetic tunnel junctions, Appl. Phys. Lett. **98**, 192111 (2011).

[15] X. Yang, J. Zheng, C.-L. Li, and Y. Guo, Spin and charge Nernst effect in a four-terminal quantum dot ring, J. Phys.: Condens. Matter **27**, 075302 (2015).

[16] S.-g. Cheng, Y. Xing, Q.-f. Sun, and X. C. Xie, Spin Nernst effect and Nernst effect in two-dimensional electron systems, Phys. Rev. B **78**, 045302 (2008).

[17] J. Li, B. Wang, F. Xu, Y. Wei, and J. Wang, Spin-dependent Seebeck effects in graphene-based molecular junctions, Phys. Rev. B **93**, 195426 (2016).

[18] Q. Wang, J. Li, Y. Nie, F. Xu, Y. Yu, and B. Wang, Pure spin current and phonon thermoelectric transport in a triangulene-based molecular junction, Phys. Chem. Chem. Phys. **20**, 15736 (2018).

[19] R. Cheng, S. Okamoto, and D. Xiao, Spin Nernst Effect of Magnons in Collinear Antiferromagnets, Phys. Rev. Lett. **117**, 217202 (2016).

[20] V. A. Zyuzin and A. A. Kovalev, Magnon Spin Nernst Effect in Antiferromagnets, Phys. Rev. Lett. **117**, 217203 (2016).

[21] J. Ziman, *Electrons and Phonons* (Oxford University Press, Cambridge, England, 1960).

[22] C. W. J. Beenakker and A. A. M. Staring, Theory of the thermopower of a quantum dot, Phys. Rev. B **46**, 9667 (1992).

[23] L.-D. Zhao, G. Tan, S. Hao, J. He, Y. Pei, H. Chi, H. Wang, S. Gong, H. Xu, V. P. Dravid, C. Uher, G. J. Snyder, C. Wolverton, and M. G. Kanatzidis, Ultrahigh power factor and thermoelectric performance in hole-doped single-crystal SnSe, Science **351**, 141 (2016).

[24] Q. Zhang, J. Liao, Y. Tang, M. Gu, C. Ming, P. Qiu, S. Bai, X. Shi, C. Uher, and L. Chen, Realizing a thermoelectric conversion efficiency of 12% in bismuth telluride/skutterudite segmented modules through full-parameter optimization and energy-loss minimized integration, Energy Environ. Sci. **10**, 956 (2017).

[25] B. Jiang, X. Liu, Q. Wang, J. Cui, B. Jia, Y. Zhu, J. Feng, Y. Qiu, M. Gu, Z. Ge, and J. He, Realizing high-efficiency power generation in low-cost PbS-based thermoelectric materials, Energy Environ. Sci. **13**, 579 (2020).

[26] Y. Xing, Q.-f. Sun, and J. Wang, Nernst and Seebeck effects in a graphene nanoribbon, Phys. Rev. B **80**, 235411 (2009).

[27] M.-M. Wei, Y.-T. Zhang, A.-M. Guo, J.-J. Liu, Y. Xing, and Q.-F. Sun, Magnetothermoelectric transport properties of multiterminal graphene nanoribbons, Phys. Rev. B **93**, 245432 (2016).

[28] D. G. Rothe, E. M. Hankiewicz, B. Trauzettel, and M. Guigou, Spin-dependent thermoelectric transport in HgTe/CdTe quantum wells, Phys. Rev. B **86**, 165434 (2012).

[29] X. Liu, D. Wang, P. Wei, L. Zhu, and J. Shi, Effect of carrier mobility on magnetothermoelectric transport properties of graphene, Phys. Rev. B **86**, 155414 (2012).

[30] J. G. Checkelsky and N. P. Ong, Thermopower and Nernst effect in graphene in a magnetic field, Phys. Rev. B **80**, 081413(R) (2009).

[31] D. Gresta, M. Real, and L. Arrachea, Optimal Thermoelectricity with Quantum Spin Hall Edge States, Phys. Rev. Lett. **123**, 186801 (2019).

[32] K. S. Novoselov, A. K. Geim, S. V. Morozov, D. Jiang, Y. Zhang, S. V. Dubonos, I. V. Grigorieva, and A. A. Firsov, Electric field effect in atomically thin carbon films, Science **306**, 666 (2004).

[33] B. Z. Rameshti and A. G. Moghaddam, Spin-dependent Seebeck effect and spin caloritronics in magnetic graphene, Phys. Rev. B **91**, 155407 (2015).

[34] N. Tombros, C. Jozsa, M. Popinciuc, H. T. Jonkman, and B. J. van Wees, Electronic spin transport and spin precession in single graphene layers at room temperature, Nature (London) **448**, 571 (2007).

[35] N. Tombros, S. Tanabe, A. Veligura, C. Jozsa, M. Popinciuc, H. T. Jonkman, and B. J. van Wees, Anisotropic Spin Relaxation in Graphene, Phys. Rev. Lett. **101**, 046601 (2008).

[36] H. Haugen, D. Huertas-Hernando, and A. Brataas, Spin transport in proximity-induced ferromagnetic graphene, Phys. Rev. B **77**, 115406 (2008).

[37] Q.-f. Sun and X. C. Xie, CT-Invariant Quantum Spin Hall Effect in Ferromagnetic Graphene, Phys. Rev. Lett. **104**, 066805 (2010).

[38] C. L. Kane and E. J. Mele, Quantum Spin Hall Effect in Graphene, Phys. Rev. Lett. **95**, 226801 (2005).

[39] Q.-f. Sun, J. Wang, and T.-h. Lin, Resonant Andreev reflection in a normal-metal–quantum-dot–superconductor system, Phys. Rev. B **59**, 3831 (1999).

[40] Q.-f. Sun, J. Wang, and T.-h. Lin, Photon-assisted Andreev tunneling through a mesoscopic hybrid system, Phys. Rev. B **59**, 13126 (1999).

[41] Q. Feng Sun and X. C. Xie, Quantum transport through a graphene nanoribbon–superconductor junction, J. Phys.: Condens. Matter **21**, 344204 (2009).

[42] D. H. Lee and J. D. Joannopoulos, Simple scheme for surface-band calculations, II. The Green's function, Phys. Rev. B **23**, 4997 (1981).

[43] M. P. L. Sancho, J. M. L. Sancho, J. M. L. Sancho, and J. Rubio, Highly convergent schemes for the calculation of bulk and surface Green functions, J. Phys. F: Metal Phys. **15**, 851 (1985).